SAR Imaging Method for Moving Target With Azimuth Missing Data

Nan Jiang , Jian Wang, Dong Feng, Naixin Kang, and Xiaotao Huang, *Senior Member, IEEE*

Abstract—To solve the problem of the moving target synthetic aperture radar (SAR) imaging from an incomplete echo, we proposed a novel SAR imaging method for the moving target with the azimuth missing data (MTIm-AMD) in this article. Instead of directly reconstructing the moving target image using the sparse SAR imaging method, we estimate and reconstruct the noncooperative moving target's complete echo from the azimuth incomplete echo based on its sparsity. At first, the noncooperative moving target's motion parameters are estimated from the incomplete echo. Then, to ensure that the complete echo can be well reconstructed using the compressed sensing method, these parameters are exploited to design a phase compensation function. Finally, using the reconstructed data, the fine-focused moving target can be obtained via the traditional SAR imaging algorithm. The simulation and experiment data results verify the effectiveness of the proposed MTIm-AMD method and demonstrate that the moving target can be fine imaging when the echo signal-to-noise ratio (SNR) is higher than -20 dB and the azimuth missing ratio (AMR) is less than 70%. This implies that the proposed MTIm-AMD method achieves satisfactory robustness to echo SNR and can handle most AMR cases.

Index Terms—Azimuth missing data (AMD), compressed sensing method, motion parameters estimation, moving target imaging.

I. Introduction

SYNTHETIC aperture radar (SAR) has been widely used in civilian and national defense fields in the past few decades [1], [2]. However, the azimuth missing data (AMD), caused by the unavoidable interference or occlusion between the moving radar and the imaging scene during the data collection processing of SAR systems, resulting Doppler loss, which severely degrades image quality if directly applying the traditional SAR imaging algorithms [3], [4].

The AMD-SAR imaging problem for the stationary imaging scene has been investigated throughout the past 20 years. In 2002, J. Salzman exploited an autoregressive linear prediction method in the SAR imaging field to deal with discontinuous aperture SAR imaging [5]. To interpolate missing data, the Burg algorithm is applied. This can achieve a satisfying imaging result

equivalent to that of the complete echo when the missing ratio is less than 30%. Although the missing ratio threshold of this method is not outstanding, it has made an important contribution to the development of AMD-SAR imaging methods. During the same period, P. Stoica and J. Li tried to extend the amplitude and phase estimation (APES) algorithm to the gapped-data APES (GAPES) one to solve the problem of the SAR imaging with the equal-gapped-data missing [6], [7], [8]. However, the GAPES algorithm is ineffective for the random AMD situation. Thus, they further proposed the missing-data APES (MAPES) algorithm based on the expectation-maximization algorithm [9]. This algorithm can effectively recover the complete echo from random AMD-SAR echo, but it also has two serious disadvantages. First, its recovery performance decreases rapidly when the missing ratio increases. Second, it has a relatively large computational complexity. To deal with the SAR imaging problem under the high missing ratios conditions, the adaptive iterative algorithm with random missing data (MIAA) algorithm was proposed in [10] in 2009. A better recovery performance has been achieved using the MIAA algorithm in the periodical or random missing data situation therein. Its recovery performance is much better than the MAPES algorithm when the missing ratio is higher than 60%, and the maximum missing ratio threshold reaches nearly 80%. However, the MIAA algorithm involves many matrix inversions and iterations, which means that the computational burden in the field of large-scene SAR imaging will be unacceptable.

In 2006, D. Donoho, E. Candés, and T. Tao proposed a cross-age compressed sensing (CS) theory based on the sparse constraints [11], [12]. This method is then applied to the field of SAR missing data imaging rapidly. Accordingly, the sparse SAR imaging methods and various corresponding variants are proposed [13], [14], [15]. However, the disadvantages of such methods are also evident. Since they directly reconstruct the strong scattering points in the scene, when the signal-to-noise ratio (SNR) of the echo is unsatisfactory, the noise becomes the strong scattering point, critically reducing the final image's accuracy.

To address this issue, Y. Qian proposed a series of AMD-SAR imaging algorithms based on sparse constraints in 2018 and 2019, respectively [16], [17]. Since this class of AMD-SAR imaging algorithms will be recurrently mentioned and compared in the following description, we will abbreviate it as AMDIA for the sake of being concise. Instead of reconstructing the strong scattering points in the scene, the AMDIA estimates and reconstructs the complete echo from the AMD echo based on the

CS method. However, the 2-D time-domain raw echo dose not satisfy the CS's sparsity prerequisite. To solve this problem, the authors in[16] discovered that, as long as the imaging scene is sparse, the raw echo's sparse representation can be achieved in the Doppler domain by multiplying the raw echo with a phase compensation function at the range frequency domain. It is worth noting that the phase compensation function is designed based on a stationary reference point, which is always the scene center point. Then, the complete echo's estimated value can be obtained after multiplying the reconstructed signal with the previous phase compensation function's conjugation. Finally, an accurate image can be obtained using traditional SAR imaging algorithms, even in a low SNR situation. Consequently, the AMDIA class has developed rapidly in the recent three years. In 2020 and 2021, K. Liu extended the AMDIA into spaceborne azimuth interrupted FMCW SAR system and gained an obvious imaging performance improvement [18], [19]. Moreover, J. Wu provided an AMD-SAR imaging method via the sparsity adaptive StOMP algorithm in 2021 based on AMDIA [3]. Compared with [16], it can provide an excellent recovery performance without any prior sparsity knowledge. In 2022, an improved AMDIA has been proposed to further accelerate AMD-SAR imaging [4]. The range compressed and range cell migration corrected echo is reconstructed instead of the raw echo's direct reconstruction. This demonstrates the computational complexity's advantage and has a better imaging performance in noiseless and noisy settings.

By reviewing the aforementioned SAR imaging algorithms with missing data, one can find that the current investigations on AMD-SAR imaging aim at the stationary sparse imaging scene. However, in the practical imaging scene, the noncooperative moving targets are inevitably included, and the SOA AMD-SAR imaging methods are not applicable. First, the moving target cannot be well-focused using the traditional moving target imaging method; this is because the AMD will lead to energy dispersion or the detection of false targets along the azimuth direction [20]. Additionally, compared with the stationary target's echo, an additional residual phase term is generated due to the motion of noncooperative moving targets. Therefore, the SOA AMDIA also cannot obtain a satisfactory moving target result.

Motivated by addressing the AMD-SAR imaging problem for the moving target and perfecting the AMDIA applicable scope, we propose an AMD-SAR imaging algorithm for moving target (MTIm-AMD) in this article. To the best of our knowledge, such a problem has not been previously investigated. First, the noncooperative moving target's motion parameters are estimated from the incomplete echo using the second-order keystone transform (SOKT) and time-frequency analysis method. The missing aperture does not affect the moving target azimuth velocity estimation. However, it leads to difficulty in estimating the moving target range velocity. According to our investigation, although the AMD echo will result in false targets or resolution reduction along the azimuth direction, an accurate estimation can still be obtained. We can determine the moving target's true position from the peak energy's position. This would consequently allow us to accurately estimate the moving target azimuth velocity based on its true position. Due to its motion effect, the residual

phase error cannot be removed via the SOA AMDIA, which significantly reduces the sparsity of the phase-compensated Doppler domain signal. Therefore, we exploit the estimated motion parameters to redesign a phase compensation function that matches the moving target model. The additional residual phase impact brought by the moving target is eliminated, guaranteeing the sparsity of the phase-compensated moving target signal at the Doppler domain. Consequently, the moving target's complete echo can be adequately reconstructed using the CS method. To eliminate potential error effects of different recovery methods, the complete echo is reconstructed using the generalized orthogonal matching pursuit (GOMP) algorithm [21], which is also the case for the SOA AMDIA class. Finally, the moving target's imaging result can be well-focused using traditional SAR imaging algorithms from the estimated complete echo and its motion parameters. This article's main innovations and contributions are summarized as follows.

1) Based on the moving target's sparsity, we proposed the MTIm-AMD method to recover the moving target's complete echo from the AMD echo. This differs from the sparse SAR imaging method that reconstructs the imaging scene's strong scattering points. The proposed MTIm-AMD method achieves satisfactory robustness to the echo SNR. Moreover, the SOA AMDIA for the stationary targets can be regarded as a special case of the proposed MTIm-AMD method. The proposed MTIm- AMD extends SOA AMDIA's applicable scope.

2) We qualitatively analyzed the effects of the moving target motion parameters on imaging performance under the AMD condition, designing an effective phase compensation function that matches the moving target model, and improving the moving target's complete echo reconstruction' accuracy.

3) We implemented several sets of SAR experiments for the moving target, and successfully verified the method's effectiveness using simulations and real measured SAR data. The results demonstrated that the proposed MTIm-AMD method can handle most azimuth missing ratio (AMR) cases, which facilitates further investigations in moving target SAR imaging.

This article is organized as follows: Section II briefly introduces the moving target's echo model. Section III derives the derivation processing of the moving target's missing data SAR imaging method in more detail. The moving target simulation and real measured SAR data results are presented in Section IV. Some important imaging performance parameters have been investigated and analyzed. Finally, Section V concludes this article.

II. SAR ECHO MODELS

The transmitted LFM signal of the radar system, $s_t(t)$, can be written as

$$s_t(t) = \beta_t \boldsymbol{w}_r(t) \exp\left(j2\pi f_c t\right) \exp\left(j\pi K_r t^2\right). \tag{1}$$

The elapsed time of the chirp signal, fast time, is represented by t. K_r denotes the chirp rate of the signal, and f_c represents the

carrier frequency. The amplitude of the chirp signal is denoted by β_t. Additionally, $\boldsymbol{w}_r(t)$ is the range windowing function.

A. Echo Model of Stationary Target With Complete Data

Accordingly, the stationary target's echo after processing the decarrier can be expressed as

$$\boldsymbol{s}_{sr}(t,\eta) = \beta_r \boldsymbol{w}_r \left(t - \frac{2\boldsymbol{R}_{sr}(\eta)}{c} \right) \boldsymbol{w}_a(\eta)$$

$$\times \exp \left\{ \frac{-j4\pi f_c \boldsymbol{R}_{sr}(\eta)}{c} \right\}$$

$$\times \exp \left\{ j\pi K_r \left(t - \frac{2\boldsymbol{R}_{sr}(\eta)}{c} \right)^2 \right\} + \boldsymbol{n}. \quad (2)$$

The time along with the synthetic aperture, slow time, is denoted by η. The back-scattered coefficient β_r can be ignored in the following derivation. The light velocity is c, and $\boldsymbol{n}$ is random noise. $\boldsymbol{w}_a(\eta)$ is the azimuth windowing function.

The slant range $\boldsymbol{R}_{sr}(\eta)$ between the stationary target and the moving radar can be demonstrated as

$$\boldsymbol{R}_{sr}(\eta) = \sqrt{x_0^2 + h^2 + (y_0 - v_a\eta)^2} \quad (3)$$

where (x_0, y_0) represents the stationary target's initial range and azimuth direction position. h is the height of the moving radar platform, and v_a represents its velocity.

B. Echo Model of Moving Target With Complete Data

However, if there is a moving target in the imaging scene, its echo after the processing of decarrier can be written as

$$\boldsymbol{s}_r(t,\eta) = \beta_r \boldsymbol{w}_r \left(t - \frac{2\boldsymbol{R}(\eta)}{c} \right) \boldsymbol{w}_a(\eta) \exp \left\{ \frac{-j4\pi f_c \boldsymbol{R}(\eta)}{c} \right\}$$

$$\times \exp \left\{ j\pi K_r \left(t - \frac{2\boldsymbol{R}(\eta)}{c} \right)^2 \right\} + \boldsymbol{n}. \quad (4)$$

It is worth noting that, compared to the stationary target situation, the slant range $\boldsymbol{R}(\eta)$ between the moving radar and target is related to the latter's 2-D velocities, which can be expressed as

$$\boldsymbol{R}(\eta) = \sqrt{(x_0 + v_x\eta)^2 + h^2 + (y_0 + (v_y - v_a)\eta)^2} \quad (5)$$

where v_x and v_y denote the value of the range and azimuth velocity of the moving target, respectively.

The Taylor approximation expansion of (5) can be extended as

$$\boldsymbol{R}(\eta) \approx R_0 + \frac{y_0^2}{2R_0} + \frac{x_0 v_x - y_0(v_a - v_y)}{R_0}\eta$$

$$+ \frac{v_x^2 + (v_a - v_y)^2}{2R_0}\eta^2 \quad (6)$$

where R_0 denotes the shortest slant range.

Since the initial azimuth position y_0 is always far less than the shortest slant range R_0, (6) can be simplified as

$$\boldsymbol{R}(\eta) \approx R_0 + \frac{x_0 v_x}{R_0}\eta + \frac{v_x^2 + (v_a - v_y)^2}{2R_0}\eta^2. \quad (7)$$
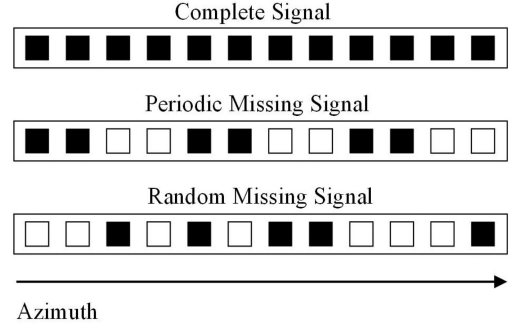

Fig. 1. Comparison between the complete, periodical missing, and random missing signals.

If R_1 and R_2 are defined as

$$R_1 \triangleq \frac{x_0 v_x}{R_0} \quad (8)$$

and

$$R_2 \triangleq \frac{v_x^2 + (v_a - v_y)^2}{R_0}. \quad (9)$$

Therefore, (7) is rewritten as

$$\boldsymbol{R}(\eta) \approx R_0 + R_1\eta + \frac{R_2}{2}\eta^2. \quad (10)$$

Compared to the stationary target situation, the moving target cannot be well-focused using the traditional SAR imaging method due to the moving target's unknown motion parameters.

C. Echo Model of MTIm-AMD

According to different types of missing data, we can define it as periodic or random missing data. Periodic AMD are usually generated by some unique SAR systems, such as the FMCW SAR system [19]. Random AMD are always caused by the influence of the interference or the occlusion [3]. Fig. 1 demonstrates the comparison between the complete signal, periodic missing signal, and random missing signal.

The black squares represent the existing samples, while the white squares represent the missing ones.

Supposing that the raw echo's full size was equal to $N_A \times N_R$, where N_A and N_R represent the number of complete samples in the azimuth and range directions, respectively. Additionally, the number of azimuth missing samples is equal to N_M ($N_M < N_A$) and $\boldsymbol{P}_m$ is the set of the positions of the azimuth missing samples. We assume that the azimuth missing matrix $\boldsymbol{\Lambda}_m$ is a diagonal matrix, which can be defined as

$$\boldsymbol{\Lambda}_m = \text{diag}\left[\lambda_{N_1}, \ldots, \lambda_{N_i}, \ldots, \lambda_{N_A} \right]. \quad (11)$$

Obviously, $\lambda_{N_i} = 0$ when $N_i \in \boldsymbol{P}_m$ and $\lambda_{N_i} = 1$ when $N_i \notin \boldsymbol{P}_m$. Thus, the raw AMD-SAR data of a moving target can be expressed as

$$\boldsymbol{s}_m(t,\eta) = \boldsymbol{\Lambda}_m \boldsymbol{s}_r(t,\eta). \quad (12)$$

By observing (12), the azimuth samples of the missing data positions are set to be zero.

Compared to the complete echo, the AMD echo will reduce the moving target's final imaging quality using the traditional moving target imaging method. Consequently, a novel moving

target imaging method has to be proposed to address the moving target AMD-SAR imaging issue.

III. SAR IMAGING METHOD FOR MTIM-AMD

The proposed moving target SAR imaging method can be divided into three parts, namely the motion parameters estimation, the complete echo recovery and moving target SAR imaging.

A. Motion Parameters Estimation

Since the motion parameters are noncooperative, the first step is to estimate its 2-D velocities from the AMD-SAR echo.

The raw AMD-SAR data of a moving target $S_m(f_r, \eta)$ at the range-frequency-azimuth-time domain can be obtained via the Fourier transform in the range direction, and it is expressed as

$$
S_m(f_r, \eta) = w_r(f_r) w_a(\eta) \exp\left(\frac{-j\pi f_r^2}{K_r}\right)
$$
$$
\times \exp\left\{\frac{-j4\pi(f_c + f_r)R(\eta)}{c}\right\}. \tag{13}
$$

After range compression, $S_{\mathrm{mrc}}(f_r, \eta)$ can be expressed as

$$
S_{\mathrm{mrc}}(f_r, \eta) = w_r(f_r) w_a(\eta) \exp\left\{\frac{-j4\pi(f_c + f_r)R(\eta)}{c}\right\}. \tag{14}
$$

Substitute (10) into upper equation, (14) can be rewritten as

$$
S_{\mathrm{mrc}}(f_r, \eta) = w_r(f_r) w_a(\eta) \exp\left\{\frac{-j4\pi(f_c + f_r)R_0}{c}\right\}
$$
$$
\times \exp\left\{\frac{-j4\pi(f_c + f_r)R_1}{c}\eta\right\} \exp\left\{\frac{-j2\pi(f_c + f_r)R_2}{c}\eta^2\right\}. \tag{15}
$$

Due to the coupling between the range frequency f_r and slow time η, the range compressed echo of the moving target shows the range walk (the second exponential term) and range curvature (the third exponential term).

To eliminate the coupling, the first time process of SOKT is introduced

$$
\eta k_1 = \sqrt{\frac{f_c + f_r}{f_c}}\eta. \tag{16}
$$

Using ηk_1 to replace slow time η and ignoring the range and azimuth window functions, the exponential term can be represented as

$$
\theta_{mk_1}(f_r, \eta k_1) = \exp\left\{\frac{-j4\pi(f_c + f_r)R_0}{c}\right\}
$$
$$
\times \exp\left\{\frac{-j4\pi\sqrt{(f_c + f_r)f_c}R_1}{c}\eta k_1\right\}
$$
$$
\times \exp\left(\frac{-j2\pi f_c R_2}{c}\eta k_1^2\right). \tag{17}
$$

Next, a time-frequency analysis method called Wigner–Ville distribution (WV-D) transformation based on selected specific range bin data is applied to estimate the Doppler chirp rate K_a[22], and then, R_2 can be obtained from

$$
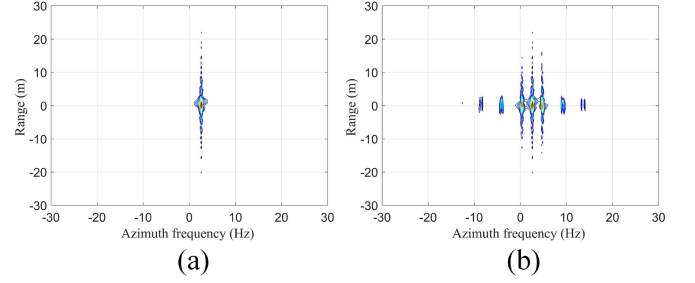R_2 = -\frac{cK_a}{4f_c}. \tag{18}
$$

Fig. 2. Imaging result using the traditional moving target imaging method from (a) complete echo and (b) echo with azimuth periodical missing data.

Therefore, the azimuth velocity of moving target v_y can be estimated by combining (9) and (18)

$$
v_y = v_a - \sqrt{2R_2 R_0 - v_x^2} \tag{19}
$$

where the range velocity v_x can be neglected due to $v_x^2 \ll 2R_2 R_0$.

A phase compensation function θ_{R_2}, which is the conjugation of the third exponential term of θ_{mk_1} is designed

$$
\theta_{R_2}(\eta k_1) = \exp\left(\frac{j2\pi f_c R_2}{c}\eta k_1^2\right). \tag{20}
$$

After the phase compensation, the result can be expressed as

$$
\theta'_{mk_1}(f_r, \eta k_1) = \exp\left\{\frac{-j4\pi(f_c + f_r)R_0}{c}\right\}
$$
$$
\times \exp\left\{\frac{-j4\pi\sqrt{(f_c + f_r)f_c}R_1}{c}\eta k_1\right\}. \tag{21}
$$

Then, to remove the range walk, the second time SOKT is applied

$$
\eta k_2 = \sqrt{\frac{f_c + f_r}{f_c}}\eta k_1. \tag{22}
$$

Using ηk_2 to replace ηk_1 in (17), a new exponential term θ_{mk_2} can be defined as

$$
\theta_{mk_2}(f_r, \eta k_2) = \exp\left\{\frac{-j4\pi(f_c + f_r)R_0}{c}\right\}
$$
$$
\times \exp\left(\frac{-j4\pi f_c R_1}{c}\eta k_2\right). \tag{23}
$$

After applying the inverse Fourier transform in the range direction and the Fourier transform in the azimuth one, respectively, the moving target can be focused in the range-time-azimuth-frequency domain. We can express the imaging result as

$$
S_{mk_2}(t, f_a) = p_r\left(t - \frac{2R_0}{c}\right) p_a\left(f_a + \frac{2f_c R_1}{c}\right)
$$
$$
\times \exp\left(\frac{-j4\pi f_c R_0}{c}\right) \tag{24}
$$

where p_r and p_a are the inverse Fourier transform of the window functions w_r and w_a, respectively, namely the Sinc function.

We can directly obtain a well-focused moving target after applying the azimuth Fourier transform if the raw echo is complete [20], as Fig. 2(a) shows. However, when the raw echo is
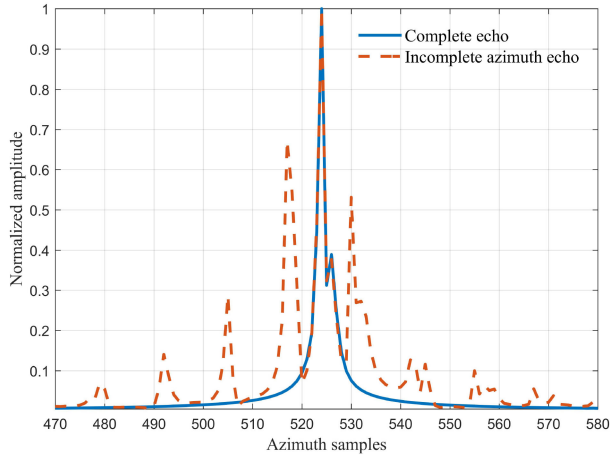
Fig. 3.   Azimuth slices obtained from the complete and azimuth incomplete echo.

incomplete, p_a in (24) cannot maintain an ideal Sinc function, resulting in the false targets of defocus along the azimuth direction. Fig. 2(b) illustrates the unsatisfactory imaging result obtained using the traditional moving target imaging method from a periodical AMD echo.

Nevertheless, we discovered that the energy peak point's azimuth position is identical to that of the real moving target under the AMD echo conditions. Fig. 3 compares the azimuth slice results of Fig. 2(a) and (b) and demonstrates the aforementioned phenomenon clearly. Hence, the correct R_1 in (24) can still be obtained by observing the azimuth position of the energy peak point, implying that v_x can be accurately estimated from the AMD echo by observing the energy peak point of the focused image.

However, the estimation accuracy of v_x suffers from AMR degradation and echo SNR degradation. More specifically, as the AMR rises, more energy from the main lobe is dispersed into the side lobes. On the other hand, when the echo SNR decreases, the noise energy may result in the energy difference between the main lobe and the side lobes to be removed. Therefore, when the aforementioned nonideal situations occur, the azimuth position of the energy peak point may no longer be equal to the azimuth position of the real moving target. A position error occurs and obviously, it will result in an inaccurate estimation of v_x. For reasons of clearness, we have skipped the introduction of estimation accuracy error effect in this section. It will be analyzed in more detail in the following description.

B. Complete Echo Recovery and SAR Imaging

The moving target's raw echo is dense in the 2-D time domain. However, motivated by the polar format algorithm, a sparser signal can be obtained in the Doppler domain by multiplying the echo signal and a phase compensation function in the range frequency domain. Thus, the CS method can be exploited to recover the moving target's complete echo. Additionally, we designed a phase compensation function based on a moving target to ensure the sparse representation. The function can be

expressed as

$$\boldsymbol{\theta}_{\text{ref}}\left(f_r, \eta\right) = \exp\left(\frac{j\pi f_r^2}{K_r}\right) \exp\left\{\frac{j4\pi\left(f_c + f_r\right)\boldsymbol{R}_{\text{ref}}\left(\eta\right)}{c}\right\} \tag{25}$$

$\boldsymbol{R}_{\text{ref}}$ denotes the slant range of the reference point. Varying from the stationary target, the moving target's estimated 2-D velocities are involved in the slant range equation, which can be expressed as

$$\boldsymbol{R}_{\text{ref}}\left(\eta\right) = \sqrt{\left(x_{\text{ref}} + v_x\eta\right)^2 + h^2 + \left(y_{\text{ref}} + \left(v_y - v_a\right)\eta\right)^2} \tag{26}$$

where $\left(x_{\text{ref}}, y_{\text{ref}}\right)$ represents the initial range and azimuth direction position of the reference point.

Accordingly, to match the raw AMD-SAR data of the moving target, the partial azimuth missing phase compensation function $\boldsymbol{\theta}_{m\text{ref}}$ can be calculated as

$$\boldsymbol{\theta}_{m\text{ref}}\left(f_r, \eta\right) = \boldsymbol{\Lambda}_m\boldsymbol{\theta}_{\text{ref}}\left(f_r, \eta\right). \tag{27}$$

Then, the phase-compensated AMD-SAR echo $\boldsymbol{S}_{m\text{pc}}(f_r, \eta)$ can be obtained by

$$\boldsymbol{S}_{m\text{pc}}(f_r, \eta) = \boldsymbol{S}_m(f_r, \eta)\boldsymbol{\theta}_{m\text{ref}}\left(f_r, \eta\right). \tag{28}$$

To successfully adopt the CS method, a small-sized signal $\boldsymbol{S}_{y\text{pc}}(f_r, \eta)$ is obtained by extracting the all-zero row vectors of $\boldsymbol{S}_{m\text{pc}}(f_r, \eta)$. The size of $\boldsymbol{S}_{y\text{pc}}(f_r, \eta)$ is equal to $N_M \times N_R$. Additionally, the phase compensated echo with azimuth complete data $\boldsymbol{S}_{\text{pc}}(f_r, \eta)$ can be expressed as

$$\boldsymbol{S}_{\text{pc}}(f_r, \eta) = \boldsymbol{S}_r(f_r, \eta)\boldsymbol{\theta}_{\text{ref}}\left(f_r, \eta\right). \tag{29}$$

Our purpose is to recover the sparse signal $\boldsymbol{S}_{\text{pc}}(t, f_a)$ from the small-sized echo $\boldsymbol{s}_{y\text{pc}}(t, \eta)$ via the GOMP algorithm. Since the GOMP algorithm is a 1-D recovery algorithm, $\boldsymbol{s}_{y\text{pc}}(t, \eta)$ needs to be divided into N_R signal vectors of N_R range cells. The signal vector of the qth range cell can be expressed as $\boldsymbol{s}_{y\text{pc}}(t_q, \eta), 1 \leq q \leq N_R$.

$\boldsymbol{s}_{y\text{pc}}(t_q, \eta)$ is regarded as the compressed signal vector $\boldsymbol{y}$, while the estimated complete signal vector $\boldsymbol{S}_{\text{pc}}(t_q, f_a)$ is regarded as the complete signal vector $\boldsymbol{x}$. Accordingly, the partial azimuth inverse Fourier transform matrix $\boldsymbol{\Phi}_{\text{PAIFT}}$ is interpreted as the sensing matrix $\boldsymbol{A}$ since $\boldsymbol{x}$ is a direct sparse signal, which means that $\boldsymbol{\Psi}$ equals the identity matrix $\boldsymbol{I}$, where the CS function is demonstrated as

$$\boldsymbol{y} = \boldsymbol{\Phi}\boldsymbol{x} = \boldsymbol{\Phi}\boldsymbol{\Psi}\boldsymbol{\alpha} = \boldsymbol{A}\boldsymbol{\alpha}. \tag{30}$$

The azimuth inverse Fourier transform matrix $\boldsymbol{\Phi}_{\text{AIFT}}$ consists of a series of row vectors $\boldsymbol{\phi}_i$, which can be defined as

$$\boldsymbol{\Phi}_{\text{AIFT}} = \left[\boldsymbol{\phi}_1, \boldsymbol{\phi}_2, \ldots, \boldsymbol{\phi}_{N_A}\right]^T. \tag{31}$$

The row vector $\boldsymbol{\phi}_i$ consisting of N_A components can be extended and (31) could be written as

$$\boldsymbol{\Phi}_{\text{AIFT}} = \frac{1}{N_A} \begin{bmatrix} \exp\left(j\frac{2\pi\eta_1\eta_1}{\eta_{N_A}}\right) & \cdots & \exp\left(j\frac{2\pi\eta_1\eta_{N_A}}{\eta_{N_A}}\right) \\ \vdots & \ddots & \vdots \\ \exp\left(j\frac{2\pi\eta_{N_A}\eta_1}{\eta_{N_A}}\right) & \cdots & \exp\left(j\frac{2\pi\eta_{N_A}\eta_{N_A}}{\eta_{N_A}}\right) \end{bmatrix}. \tag{32}$$

The size of $\boldsymbol{\Phi}_{\text{AIFT}}$ is $N_A \times N_A$.

Similarly to (12) and (27), the missing azimuth inverse Fourier transform matrix $\boldsymbol{\Phi}_{m\text{AIFT}}$ can be calculated as

$$\boldsymbol{\Phi}_{m\text{AIFT}} = \boldsymbol{\Lambda}_m\boldsymbol{\Phi}_{\text{AIFT}}. \tag{33}$$
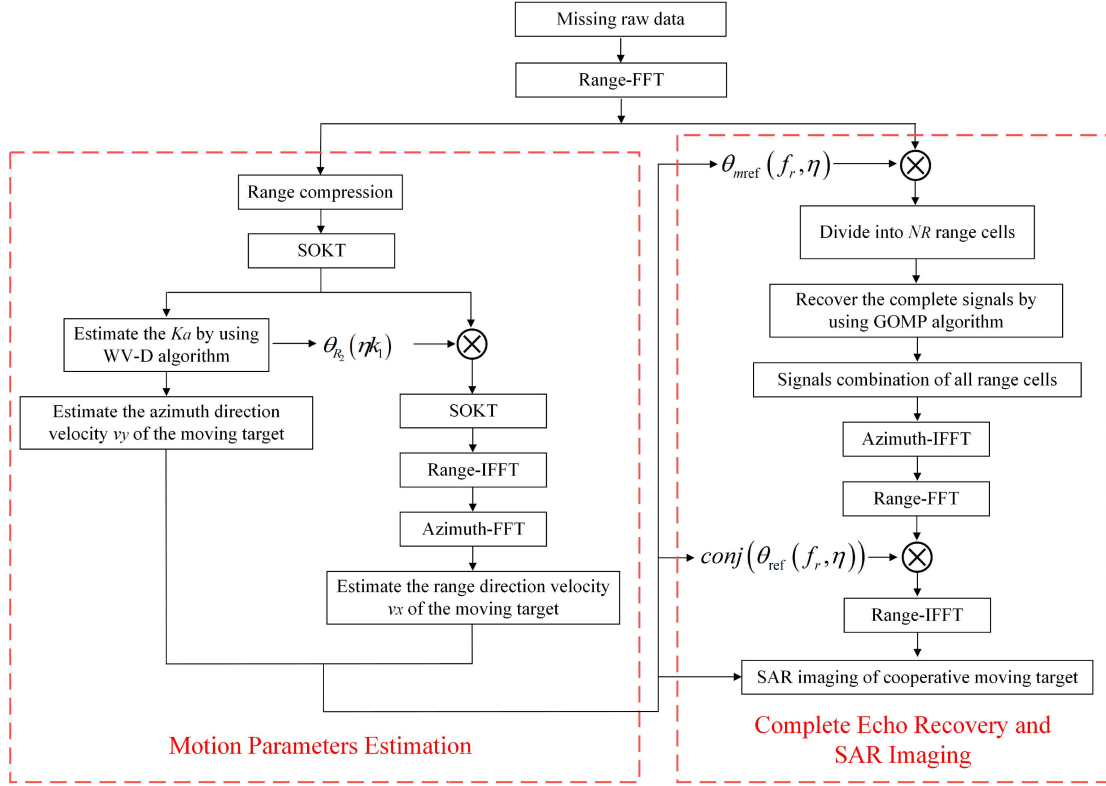
Fig. 4. Flowchart of the proposed MTIm-AMD method.

When the all-zero row vectors of $\mathbf{\Phi}_{m\text{AIFT}}$ are extracted, the partial azimuth inverse Fourier transform matrix $\mathbf{\Phi}_{\text{PAIFT}}$, having a size of $N_M \times N_A$, is realized.

Thus, the complete signal recovery problem can be solved using the following equation:

$$\min_{\mathbf{S}_{\text{pc}}(t_q, f_a)} ||\mathbf{S}_{\text{pc}}(t_q, f_a)||_1$$

$$\text{s.t. } ||\mathbf{\Phi}_{\text{PAIFT}}\mathbf{S}_{\text{pc}}(t_q, f_a) - \mathbf{s}_{y\text{pc}}(t_q, \eta)||_2 \leq T_s \quad (34)$$

where T_s is the threshold parameter. Then, the estimated complete signal of qth range cell $\hat{\mathbf{S}}_{\text{pc}}(t_q, f_a)$ is reconstructed via the GOMP algorithm. After combining the signals of all recovered range cells, the estimated complete echo $\hat{\mathbf{S}}_{\text{pc}}(t, f_a)$ in the range-time-azimuth-frequency domain can be obtained.

Since $\hat{\mathbf{S}}_{\text{pc}}(t, f_a)$ is the phase compensated echo, to receive the estimation value of real complete echo $\hat{s}_r(t, \eta)$, the conjugate phase compensation function should be compensated in the range-frequency-azimuth-time domain. We can express that, as

$$\hat{\mathbf{S}}_r(f_r, \eta) = \hat{\mathbf{S}}_{\text{pc}}(f_r, \eta)\text{conj}(\boldsymbol{\theta}_{\text{ref}}(f_r, \eta)) \quad (35)$$

where $\text{conj}(\cdot)$ denotes the conjugate operation. Therefore, the complete recovered echo $\hat{s}_r(t, \eta)$ of a moving target can be obtained after processing of the inverse Fourier transform in the range direction. Finally, since the moving target's 2-D velocities and complete echo are known, we can observe it as a cooperative target. It can be adequately focused using traditional SAR imaging algorithms.

Furthermore, it worth noting that when the motion parameter estimation is inaccurate, it will cause a residual phase error between the phase compensation function generated by the incorrect estimated motion parameters and the real moving target phase. Excessive residual phase error will reduce the sparsity of the phase-compensated signal in the sparse domain, thus reducing the reconstruction accuracy of the full aperture echo of the moving target. The obtained imaging result from an inaccurately reconstructed complete echo will be defocused. However, estimating motion parameters under the worst echo conditions is not the main focus of this article. Thus, we assume that this phase error is within a reasonable range in this article.

The flowchart of the proposed MTIm-AMD method is demonstrated in Fig. 4. The SAR raw data-based GOMP algorithm's detailed steps are more thoroughly introduced in the following subsection.

C. GOMP Algorithm

In 2012, an extension of the OMP algorithm, namely the GOMP algorithm, was proposed to pursue a superior reconstruction performance when it comes to recovering sparse signals [21]. The algorithm's main principle is obtaining an estimated value of the reconstructed signal $\boldsymbol{x}$ by using the least-square method. $\mathbf{S}_{\text{pc}}(t_q, f_a)$ is regarded as the reconstructed signal $\boldsymbol{x}$ in the complete echo reconstruction process.

First, the sensing matrix $\mathbf{\Phi}_{\text{PAIFT}}$, the observed compressed signal $\mathbf{s}_{y\text{pc}}(t_q, \eta)$, the threshold parameter T_s, and the maximum number of iterations $I_{\max}$ are given. Next, let the initial iteration parameter $It = 1$, initial residual $\boldsymbol{r}^0 = \boldsymbol{y}$, and set a new sensing matrix $\boldsymbol{B}^0 = \emptyset$.

The GOMP algorithm finds P basis column vectors that most contribute to the compressed signal vector $\boldsymbol{s}_{ypc}(t_q, \eta)$ in each iteration, that is

$$\text{product} = \left\langle \boldsymbol{r}^{It-1}, \boldsymbol{a}_i \right\rangle, \ 1 \leq It \leq I_{\max}. \tag{36}$$

Then, the values of products are sorted from the largest to smallest. The largest P values are picked, which can then be expressed as

$$\boldsymbol{a}_{\max_p} = \arg\max |\text{product}|, \ 1 \leq p \leq P \tag{37}$$

where $|\cdot|$ represents the absolute value operation. Trivially, the GOMP algorithm becomes the OMP one when $P = 1$. Then, $\boldsymbol{B}^{It}$ can be updated by

$$\boldsymbol{B}^{It} = \boldsymbol{B}^{It-1} \cup \left[\boldsymbol{a}_{\max_1}, \ldots, \boldsymbol{a}_{\max_P} \right]. \tag{38}$$

Moreover, the current least-squares solution $\hat{\boldsymbol{\alpha}}$ can be solved by

$$\min_{\hat{\boldsymbol{\alpha}}} ||\boldsymbol{B}^{It} \hat{\boldsymbol{\alpha}} - \boldsymbol{y}||_2 \tag{39}$$

which means that $\hat{\boldsymbol{\alpha}}$ can be calculated as

$$\hat{\boldsymbol{\alpha}} = \left(\left(\boldsymbol{B}^{It} \right)^T \boldsymbol{B}^{It} \right)^{-1} \left(\boldsymbol{B}^{It} \right)^T \boldsymbol{y} \tag{40}$$

where T represents the transpose operation.

Finally, the current residual $\boldsymbol{r}^{It}$ can be obtained by

$$\boldsymbol{r}^{It} = \boldsymbol{y} - \boldsymbol{B}^{It} \hat{\boldsymbol{\alpha}}. \tag{41}$$

The iteration is terminated only when the residual $\boldsymbol{r}^{It}$ meets the stopping condition, such as $It = I_{\max}$, $\boldsymbol{r}^{It} = 0$ or $\boldsymbol{r}^{It} \leq Ts$. Otherwise, the iteration parameter should be updated

$$It = It + 1. \tag{42}$$

When the iteration stops, $\hat{\boldsymbol{\alpha}}$ can be regarded as an effective estimation of $\boldsymbol{S}_{pc}(t, f_a)$. The signal reconstruction is accomplished.

IV. EXPERIMENT RESULTS AND ANALYSIS

To verify the effectiveness of the proposed AMD-SAR imaging method for moving target, some simulations and SAR experiments for the moving target were designed and conducted.

A. Verification of the Proposed Moving Target Imaging Method

Compared to the random AMD-SAR imaging results, the false targets are more prominent in the periodic missing data. Thus, to further illustrate the proposed method's imaging performance advantage more clearly, we assume that the missing type is periodic in the first simulation. There are 16 existing azimuth samples after 16 missing samples, which means that $AMR = 50\%$. The key parameters for the simulations are shown in Table I. First, four imaging results are shown in Fig. 5.

Since the 2-D velocities of the moving target are unknown, the imaging result appears to defocus and displace along the azimuth direction. Moreover, as shown in Fig. 5(a), the results are aliasing due to the AMD.

Fig. 5(b) demonstrates the periodic missing data imaging result using the traditional moving target SAR imaging method. The traditional moving target SAR imaging method mentioned in this article includes four steps: the first SOKT, the time-frequency analysis, the second SOKT, and the azimuth fast

TABLE I
KEY PARAMETERS FOR SIMULATIONS

| Parameters	Value
Central frequency / f_c	1 GHz
Shortest central slant range / R_c	2864 m
Signal frequency bandwidth / B	100 MHz
Range sampling rate / f_s	200 MHz
Pulse repetition frequency / PRF	176 Hz
Range samples / N_R	296
Azimuth samples / N_A	1024
Velocity of radar / v_a	100 m/s
Range velocity of moving target / v_x	2 m/s
Azimuth velocity of moving target / v_y	3 m/s
Initial position of moving target	(0, 0)
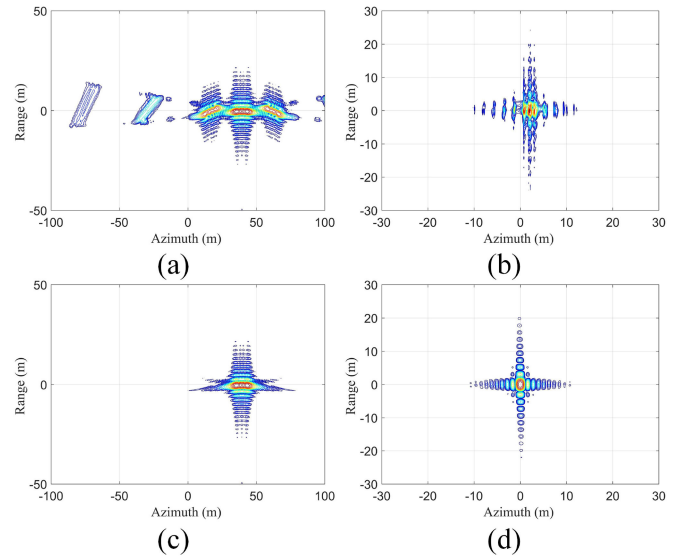
Fig. 5. Moving target imaging result obtained from the periodic AMD echo using (a) traditional stationary target imaging method, (b) traditional moving target SAR imaging method, (c) SOA AMDIA, and (d) proposed MTIm-AMD method.

Fourier transform [20]. Since the azimuth fast Fourier transform process is directly applied in the AMD echo, some ghost targets appear in Fig. 5(b). This implies that the traditional moving target imaging method cannot effectively focus on the moving target when there are some gaps along the azimuth direction.

The focused contour picture of the moving target using proposed method is shown in Fig. 5(d), and the focused contour picture of the moving target by using SOA AMDIA is shown in Fig. 5(c). By comparing Fig. 5(c) and (d), we can find that the SOA AMDIA can only eliminate the ghost targets. However, its focusing ability is still unacceptable. In contrast, since the moving target's motion parameters are involved in the complete
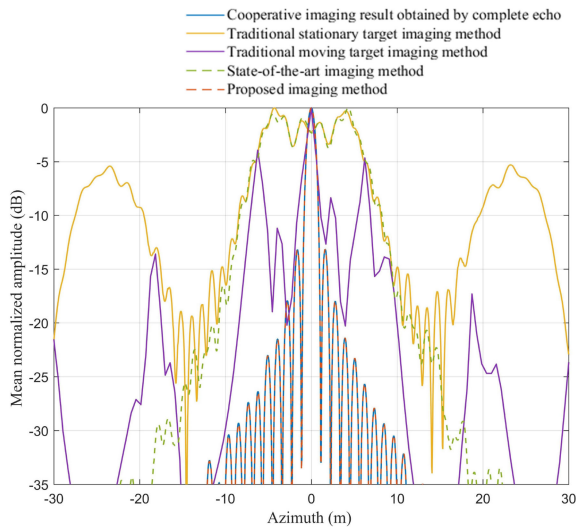
Fig. 6. Azimuth slices obtained by using different imaging methods. The blue solid line represents the azimuth slice of the cooperative imaging result obtained by complete echo, the yellow solid line represents the azimuth slice of the noncooperative moving target with AMD using the traditional stationary target imaging method, the purple solid line represents the azimuth slice of the noncooperative moving target with AMD using the traditional moving target imaging method, the green dotted line represents the azimuth slice of the noncooperative moving target with AMD using the SOA AMDIA, and the red dotted line represents the azimuth slice of the noncooperative moving target with AMD using the proposed MTIm-AMD method.

TABLE II
RELATED IMAGING PERFORMANCE PARAMETERS OBTAINED BY USING
DIFFERENT IMAGING METHODS

Imaging Method	IRW (m)	PSLR (dB)
Cooperative Imaging Result obtained by Complete Echo	1.016	-13.20
Traditional Stationary Target Imaging Method with AMD	11.615	-5.41
Traditional Moving Target Imaging Method with AMD	0.920	-3.93
SOA AMDIA	11.567	N/A
Proposed MTIm-AMD Method	1.016	-13.24

echo's reconstruction, the proposed method achieves fine imaging performance, successfully verifying the proposed method's effectiveness.

To further demonstrate the advantage of the proposed MTIm-AMD method, the imaging results' azimuth slices are shown in Fig. 6.

The method can obtain an almost identical result as the cooperative imaging result obtained by complete echo. The moving target's related imaging performance parameters, such as the azimuth impulse response width (IRW) and the peak side lobe ratio (PSLR) are shown in Table II. Due to the widening of the main lobe, the side lobes obtained using SOA AMDIA disappear. Therefore, the target's PSLR using SOA AMDIA was not analyzed.

Compared to the imaging result of the traditional stationary target imaging method with AMD echo, the azimuth IRW vastly

improved from 11.615 to 1.016 m using the proposed MTIm-AMD method. Accordingly, the azimuth PSLR decreases from -5.41 to -13.24 dB, implying an eminent imaging performance improvement. Furthermore, although the IRW of the imaging result obtained using the traditional moving target imaging method was slightly better than our method, the PSLR, which was equal to -3.93 dB, was unacceptable.

Therefore, the imaging performance of the traditional moving target imaging method is still worse when the echo is incomplete. The advantage of the proposed method is evident, and the moving target imaging in the AMD situation problem has been solved.

B. Imaging Performance Effects of Different Echo SNR

To thoroughly investigate the proposed MTIm-AMD method's effectiveness in noisy environments, we designed and implement a series of simulations based on different echo SNRs. The missing type is identical to the Section IV-A. AMR is equal to 50%. It is worth mentioning that the 2-D velocities of the moving target cannot be effectively estimated when the SNR is less than -20 dB. Therefore, we only explore the method's effectiveness when the echo SNR is greater than -20 dB. The imaging results obtained from the proposed MTIm-AMD method under different SNRs conditions are shown in Fig. 7.

By observing Fig. 7, although the low echo SNR causes high clutter in the final imaging result, a well-focused moving target can still be observed using the proposed method even if the SNR was equal to -20 dB. This result demonstrates a considerable advantage: the proposed MTIm-AMD method achieves satisfactory robustness to the echo SNR.

Moreover, the IRW of the imaging results obtained using different imaging methods under varying SNRs conditions is illustrated in Fig. 8.

In all different SNR situations, the proposed MTIm-AMD method ensures that the azimuth IRW is identical to that of the cooperative imaging result obtained by complete echo, which is equal to 1.016 m. Contrarily, the SOA AMDIA cannot improve the azimuth IRW. This implies that the proposed MTIm-AMD method is not sensitive to the echo SNR and can obtain an ideal IRW even if the echo SNR is low. Additionally, the moving target using the traditional moving target imaging method can reach a slightly better azimuth IRW than the cooperative imaging result obtained by complete echo, as the yellow solid line shows. However, it creates some high side lobes, as shown in Fig. 5(b).

The PSLR results are shown in Fig. 9, which has the same legend as Fig. 8. As mentioned previously, the PSLR of the imaging result focused on using the SOA AMDIA has not been analyzed.

At first, as demonstrated by the yellow solid line, the traditional moving target imaging method with the AMD achieved the worst azimuth PSLR. This implies that the final imaging result is still unacceptable. Additionally, compared to the moving target's PSLR using the traditional imaging method of the stationary target, the azimuth PSLR was reduced by almost 8 dB using the proposed MTIm-AMD method. When the echo SNR was higher than -15 dB, the azimuth PSLR obtained using the
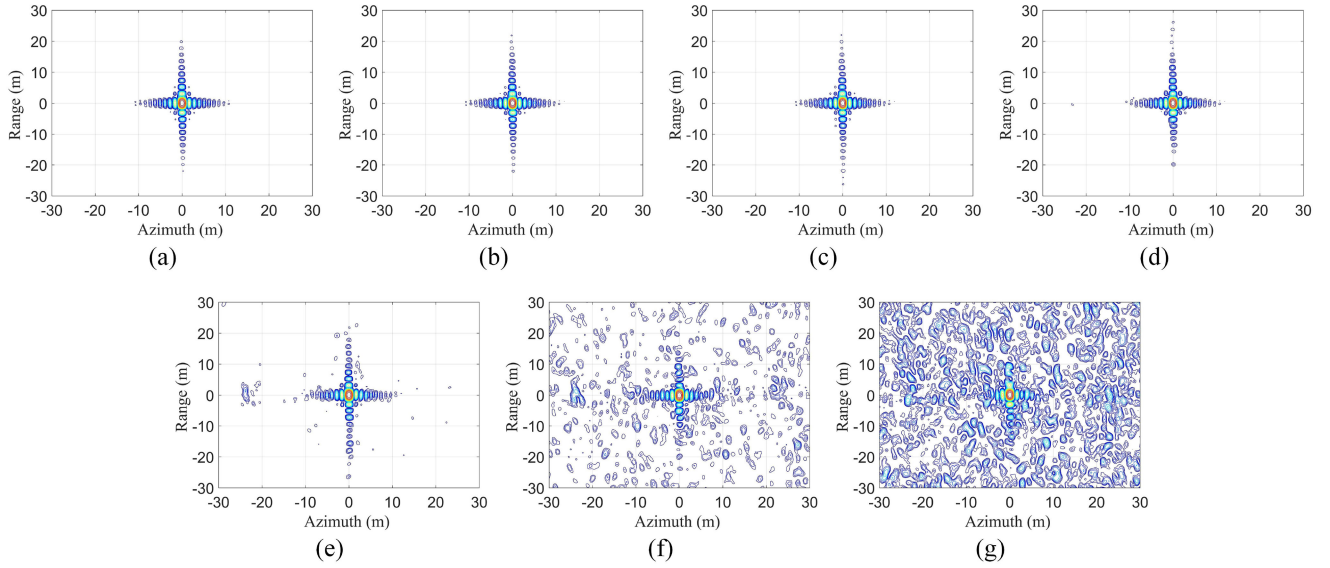
Fig. 7.   Imaging results obtained using the proposed MTIm-AMD method under different SNRs conditions. (a) SNR = 10 dB. (b) SNR = 5 dB. (c) SNR = 0 dB. (d) SNR = −5 dB. (e) SNR = −10 dB. (f) SNR = −15 dB. (g) SNR = −20 dB.
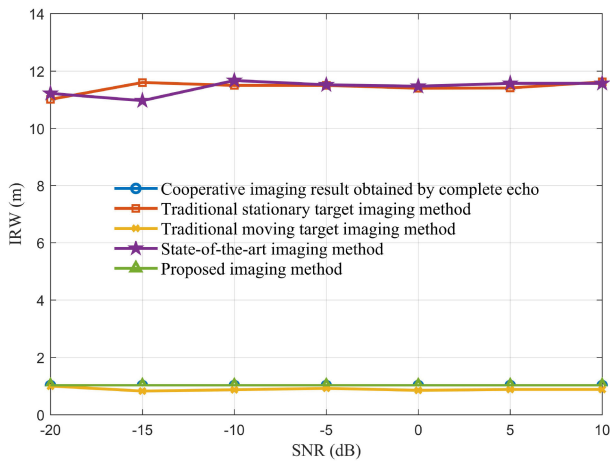

Fig. 8.   Azimuth IRW obtained by using the different imaging methods under the conditions of the different SNR. The blue solid line with circles represents the azimuth IRW of the cooperative imaging result obtained by complete echo, the red solid line with squares represents the azimuth IRW of the imaging result of the noncooperative moving target with AMD using the traditional stationary target imaging method, the yellow solid line with ×s represents the azimuth IRW of the imaging result of the noncooperative moving target with AMD using the traditional moving target imaging method, the purple solid line with stars represents the azimuth IRW of the imaging result obtained using the SOA AMD imaging method, and the green solid line with triangles represents the azimuth IRW of the imaging result obtained using the proposed AMD imaging method.
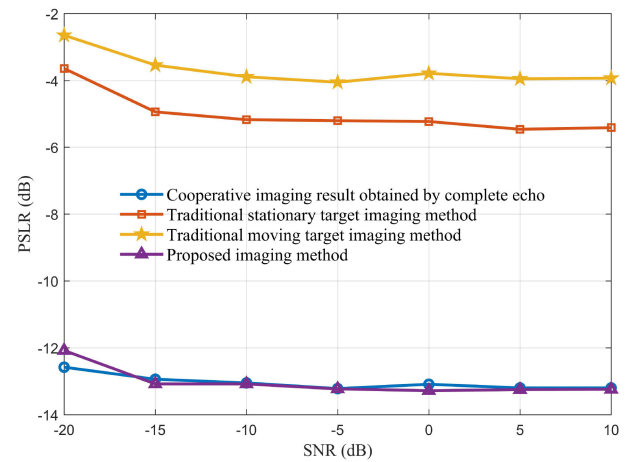
Fig. 9.   Azimuth PSLR obtained by using the different imaging methods under the conditions of the different SNR. The blue solid line with circles represents the azimuth PSLR of the cooperative imaging result obtained by complete echo, the red solid line with squares represents the azimuth PSLR of the imaging result of the noncooperative moving target with AMD using the traditional stationary target imaging method, the yellow solid line with stars represents the azimuth PSLR of the imaging result obtained using the SOA AMD imaging method, and the purple solid line with triangles represents the azimuth PSLR of the imaging result obtained using the proposed AMD imaging method.

under the various SNRs. The method's effectiveness in noisy environments has been verified once more.

C. Imaging Performance Effects of Different Azimuth Missing Ratios

Furthermore, to investigate the applicable limitation of the proposed MTIm-AMD method, a series of moving target simulations based on different AMRs were designed and implemented. Without loss of generality, with the increase of AMR, the final imaging performance of the traditional moving target SAR
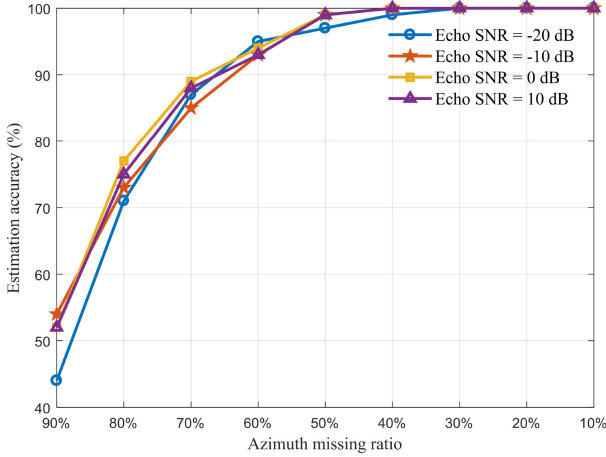
proposed MTIm-AMD method was almost identical to that of the cooperative imaging result obtained by complete echo, which was approximately equal to −13.2 dB. Although there is a 0.5-dB difference in the PSLR between the cooperative imaging result obtained by complete echo and the proposed MTIm-AMD imaging result when the echo SNR was equal to −20 dB, it is still tolerable.

Therefore, the proposed MTIm-AMD method can significantly improve the AMD-SAR moving target's imaging quality

Fig. 10. Estimation accuracy of v_x under different AMRs conditions. The blue solid line with circles represents the results when the echo SNR $= -20$ dB, the red solid line with stars represents the results when echo SNR $= -10$ dB, the yellow solid line with squares represents the results when the echo SNR $= 0$ dB, and the purple solid line with triangles represents the results, then the echo SNR $= 10$ dB.

Fig. 11. Mean Δv_x under the conditions of different AMRs. The blue solid line with circles represents the results when the echo SNR $= -20$ dB, the red solid line with stars represents the results when echo SNR $= -10$ dB, the yellow solid line with squares represents the results when the echo SNR $= 0$ dB, and the purple solid line with triangles represents the results when the echo SNR $= 10$ dB.

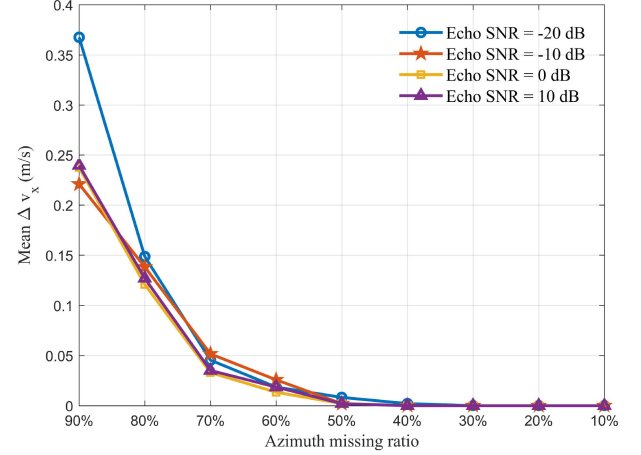Fig. 12. Maximum Δv_x under the conditions of different AMRs. The blue solid line with circles represents the results when the echo SNR $= -20$ dB, the red solid line with stars represents the results when echo SNR $= -10$ dB, the yellow solid line with squares represents the results when the echo SNR $= 0$ dB, and the purple solid line with triangles represents the results, then the echo SNR $= 10$ dB.
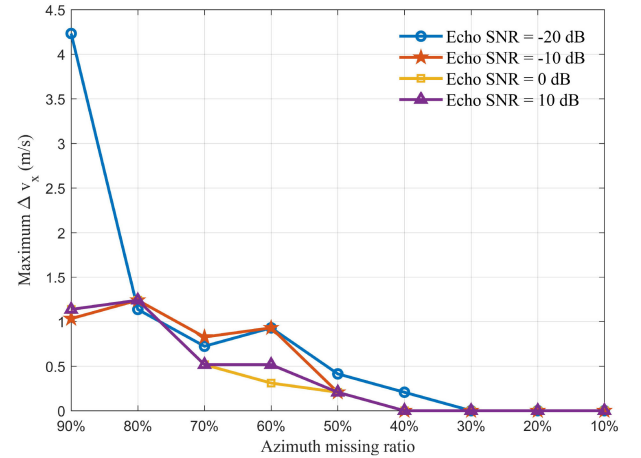
imaging method degraded. This implies that the estimation accuracy of the range velocity v_x may be affected. The estimation accuracy of the range velocity under different AMRs and SNRs is illustrated in Fig. 10, and the results were obtained using 100 Monte-Carlo trials.

The estimation accuracy decreases significantly when the AMR increases in all SNR situations. When the AMR was equal to 60%, the estimation accuracy of the range velocity v_x can still be around 95% in all SNR situations. However, once the AMR becomes higher than 70%, the range velocity's estimation accuracy rapidly drops into the unacceptable range. Additionally, as shown in Fig. 10, we can find that the echo SNR's influence on the estimation accuracy was not obvious when the AMR was low. However, once the AMR becomes extremely high, we should consider the impact of the worse echo SNR. Specifically, the estimation accuracy was only 44% when the AMR was equal to 90% and the echo SNR was equal to -20 dB.

The value difference between the estimated and real range velocity will affect the proposed MTIm-AMD method's imaging performance. The value difference Δv_x can be calculated as

$$\Delta v_x = |\hat{v}_x - v_x| \tag{43}$$

where $|\cdot|$ represents the absolute value operation.

First, the mean Δv_x has been calculated based on different AMRs. The main purpose is to determine the approximate scope of estimation v_x error, and then, further investigate the general imaging performance impact brought by the average estimation error under the conditions of different AMRs. The related results are demonstrated in Fig. 11.

The mean Δv_x increases when the AMR climbs in all SNR situations. There is no significant correlation between the value of the mean Δv_x and the echo SNR. Only when the AMR and the echo SNR are significantly worse, the mean Δv_x show a rapid deterioration that was equal to 0.37 m/s.

However, the mean Δv_x can only be used to measure the estimation error from a global perspective. Additionally, to explore the estimation error's maximum impact, the maximum Δv_x caused by the different AMRs should be considered. The related results are shown in Fig. 12.

From Fig. 12, we can derive almost identical conclusions as those obtained from Fig. 11. Overall, a larger maximum Δv_x emerges in the high AMR situation. However, the variation of the maximum Δv_x is not linear with the change in the AMR. For example, as the red solid line with stars shows, when the echo SNR was equal to -10 dB, the maximum Δv_x was equal to 0.93, 0.83, 1.24, and 1.03 m/s under the conditions of 60%, 70%, 80%, and 90% azimuth missing, respectively. Moreover, there is no significant correlation between the value of the maximum Δv_x and the echo SNR. The greatest maximum Δv_x was obtained
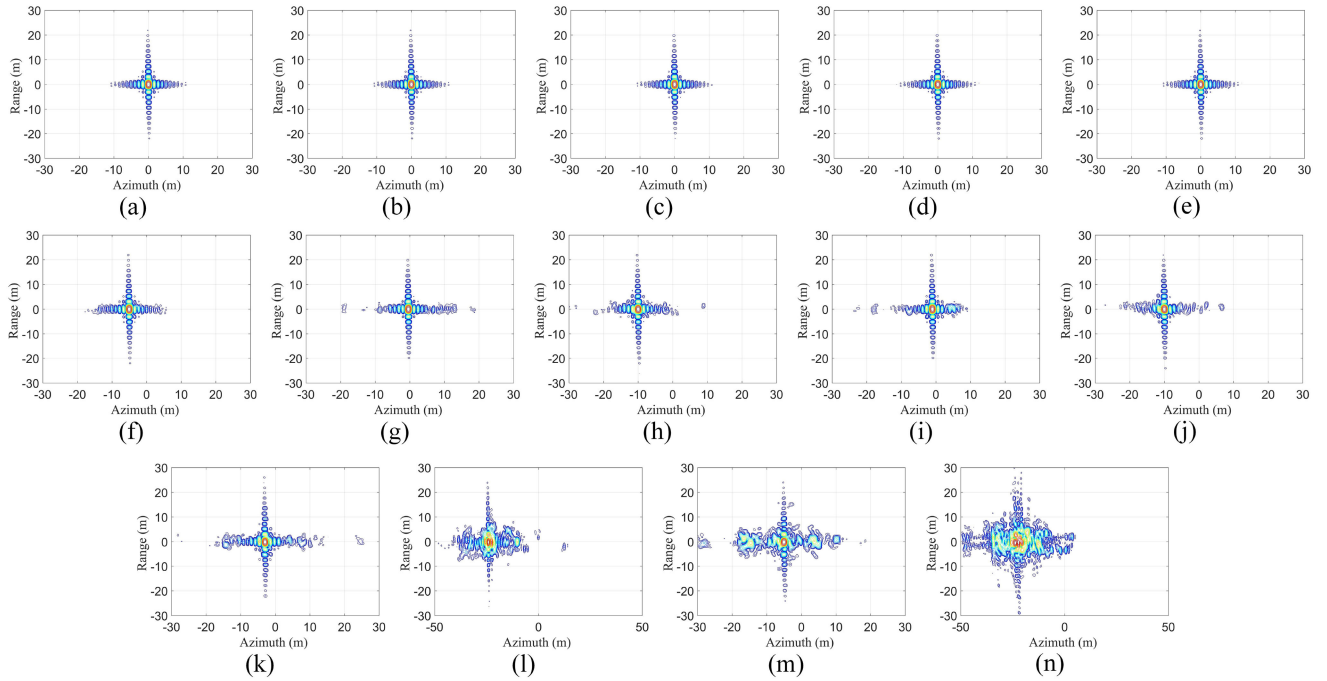
Fig. 13. Imaging results obtained by using the proposed MTIm-AMD method under the conditions of different AMRs when echo SNR = 10 dB. (a) AMR = 10%. (b) AMR = 20%. (c) AMR = 30%. (d) AMR = 40%. (e) AMR = 50% with mean(Δv_x). (f) AMR = 50% with max(Δv_x). (g) AMR = 60% with mean(Δv_x). (h) AMR = 60% with max(Δv_x). (i) AMR = 70% with mean(Δv_x). (j) AMR = 70% with max(Δv_x). (k) AMR = 80% with mean(Δv_x). (l) AMR = 80% with max(Δv_x). (m) AMR = 90% with mean(Δv_x). (n) AMR = 90% with max(Δv_x).

when the echo SNR was equal to -20 dB and the AMR was 90%. This conclusion is the same as the previous study on the mean Δv_x.

When the moving target's range velocity estimation accuracy was clarified, the proposed method's applicable limitation can be deeply investigated by observing Fig. 13.

Fig. 13 illustrates the number of imaging results obtained using the proposed MTIm-AMD method under various AMRs conditions when the echo SNR was equal to 10 dB. Since there was no estimation error of range velocity of the moving target when the AMR was less than 40%, the imaging performance comparison of imaging results caused by the mean and maximum Δv_x were displayed only when the AMR was higher than 40%. This is shown in Fig. 13(e)–(n). Furthermore, the detailed azimuth IRW and PSLR are, respectively, demonstrated in Figs. 14 and 15.

According to the pictures, we found that the imaging performance was impeccable when the AMR was less than 40% compared to the azimuth IRW and PSLR of cooperative imaging result obtained by complete echo. Additionally, although the estimation error of v_x may generate when the missing rate is higher than 40% and less than 70%, the proposed MTIm-AMD method can still adequately focus on the moving target even in the maximum Δv_x situation. Compared to the imaging result obtained using the traditional moving target imaging method, a considerable imaging performance advantage can be observed in Figs. 14 and 15 when the AMR was less than 70%.

However, when the AMR reaches 80%, although the final imaging result is tolerable with the mean Δv_x, the maximum Δv_x resulted in a rapidly increasing PSLR. The unacceptable
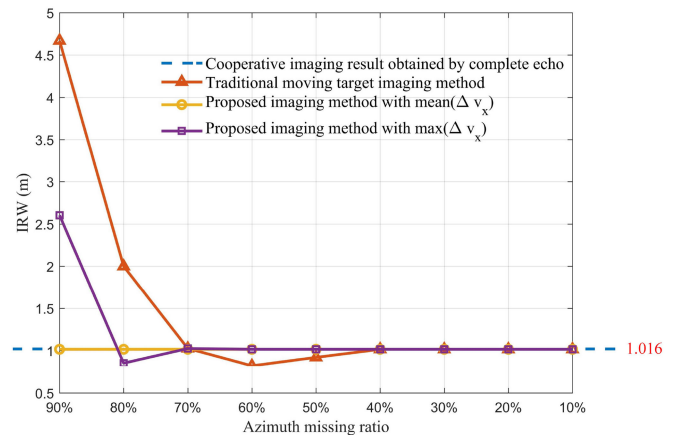

Fig. 14. Azimuth IRW obtained by using the proposed MTIm-AMD method under the conditions of the different AMRs when echo SNR = 10 dB. The blue dotted line represents the azimuth IRW of the cooperative imaging result obtained by complete echo, which is a constant and equal 1.016 m, the red solid line with triangles represents the azimuth IRW of the noncooperative moving target with AMD using the traditional moving target imaging method, the yellow solid line with circles represents the azimuth IRW of the imaging result obtained using the proposed MTIm-AMD method with mean Δv_x, and the purple solid line with squares represents the azimuth IRW of the imaging result obtained using the proposed MTIm-AMD method with maximum Δv_x.

result can be found in Fig. 13(l). As shown in Fig. 13(m), when the AMR climbed to 90%, the ghost targets can be clearly observed; this also held even when the estimation error was equal to mean Δv_x. When the estimation error was equal to maximum Δv_x, the azimuth IRW and PSLR were significantly unsatisfactory, in which they were equal to 2.6 m and -3.50 dB,
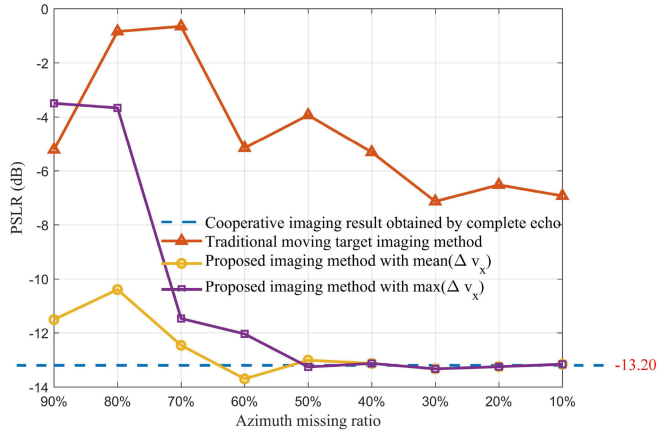
Fig. 15. Azimuth PSLR obtained by using the proposed MTIm-AMD method under the conditions of the different AMRs when echo SNR = 10 dB. The blue dotted line represents the azimuth PSLR of the cooperative imaging result obtained by complete echo, which is a constant and equal -13.20 dB, the red solid line with triangles represents the azimuth PSLR of the noncooperative moving target with AMD using the traditional moving target imaging method, the yellow solid line with circles represents the azimuth PSLR of the imaging result obtained using the proposed MTIm-AMD method with mean Δv_x, and the purple solid line with squares represents the azimuth PSLR of the imaging result obtained using the proposed MTIm-AMD method with maximum Δv_x.

Fig. 16. 77-GHz millimeter-wave SAR system for the real measured experiment. The electric rail length equals 1.57 m and the radar height equals 1.40 m.

respectively. We can also find that a worse estimation of v_x will result in a worse final imaging result obtained via the proposed MTIm-AMD method by comparing Fig. 13(k) and (l), and (m) and (n).

Thus, we can conclude that the proposed MTIm-AMD method was ineffective only when the AMR was higher than 70%, implying that it could handle most AMD cases.

D. Real Measured Data Processing Results

To further investigate the theoretical analysis presented in this article, we conducted some experiments for the moving target. A 77-GHz millimeter-wave radar was settled in an electric rail, as shown in Fig. 16. The signal bandwidth is 3 GHz. The complete 2-D raw data size was 1024×1960 (Range samples $\times$ Azimuth samples). Assuming the AMD real measured echo is generated by a periodic gap every 40 pulses, thus the size of the AMD echo is 1024×980, which means that the AMR = 50%. Moreover, a triangle reflector was installed in another electric rail as a noncooperative moving target in the imaging scene. The moving
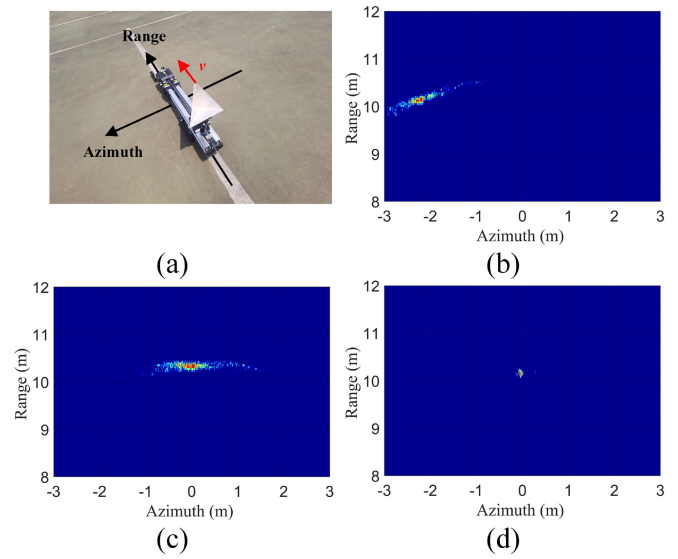

Fig. 17. (a) Imaging scene of motion case 1. (b) Imaging result obtained using the traditional stationary target imaging method with AMD echo. (c) Imaging result obtained using the SOA AMD-SAR imaging method. (d) Imaging result obtained using the proposed MTIm-AMD method with AMD echo.

target velocity was $v_{mt} = 0.65$ cm/s and the initial position of the moving target was $P_{mt}(10, 0)$.

Suppose that the moving target moves at a uniform speed along the range direction as motion case 1, along the azimuth direction as motion case 2, and along the 2-D directions as motion case 3. The real measured SAR experiments for motion cases 1–3 are carefully designed. In motion case 1, $v_x = v_{mt}$ and $v_y = 0$. In motion case 2, $v_x = 0$ and $v_y = v_{mt}$. In motion case 3, $v_x = v_{mt} \sin(3\pi/4)$ and $v_y = v_{mt} \cos(3\pi/4)$.

Fig. 17(a) displays the imaging scene of motion case 1 and Fig. 17(b)–(d) illustrate the moving target imaging results of the three different imaging methods, respectively. Due to the unknown residual phase error effect of the noncooperative moving target, the SOA AMDIA cannot accurately reconstruct the well-imaged moving target; this is demonstrated in Fig. 17(c). Compared with the imaging result obtained using the traditional stationary target SAR and the SOA AMD-SAR imaging methods, the proposed MTIm-AMD imaging method can significantly improve the moving target's imaging performance in the AMD echo situation, as shown in Fig. 17(d).

Moreover, the imaging scenes and the related imaging results of motion cases 2 and 3 are demonstrated in Figs. 18 and 19, respectively. Figs. 18(d) and 19(d) obtained the best focus quality, implying that the proposed MTIm-AMD method can greatly enhance the moving target imaging performance under AMD echo conditions. This further validates the proposed MTIm-AMD method's effectiveness using real measured SAR data.

Moreover, to quantitatively evaluate the imaging performance of the proposed MTIm-AMD method, the image entropy (IE) is introduced to determine the final imaging results' focus degree. The lower the IE value, the better the focus of the image. The IE results are shown in Table III and the best values obtained by
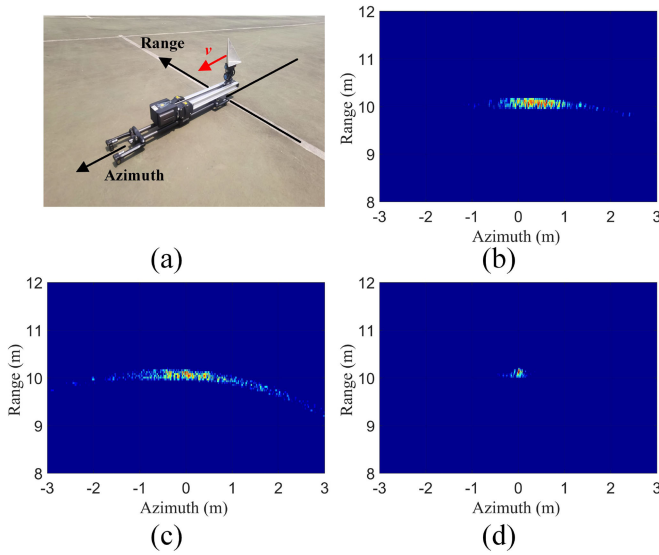
Fig. 18. (a) Imaging scene of motion case 2. (b) Imaging result obtained using the traditional stationary target imaging method with AMD echo. (c) Imaging result obtained using the SOA AMD-SAR imaging method. (d) Imaging result obtained using the proposed MTIm-AMD method with AMD echo.
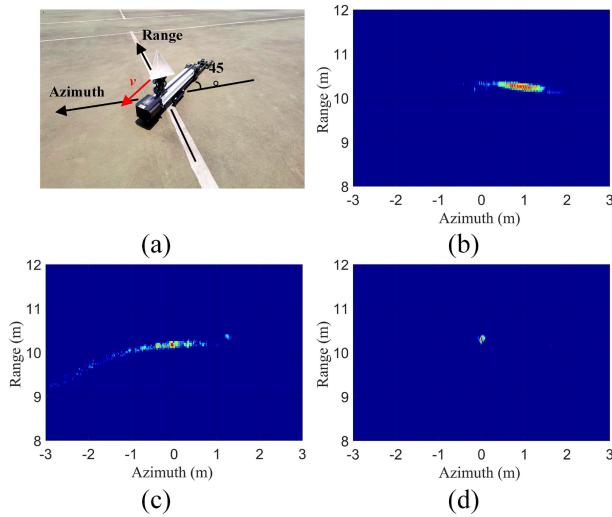

Fig. 19. (a) Imaging scene of motion case 3. (b) Imaging result obtained using the traditional stationary target imaging method with AMD echo. (c) Imaging result obtained using the SOA AMD-SAR imaging method. (d) Imaging result obtained using the proposed MTIm-AMD method with AMD echo.

TABLE III
IE RESULTS OBTAINED USING DIFFERENT IMAGING METHODS IN DIFFERENT MOTION CASES

Imaging Methods	Motion case 1	Motion case 2	Motion case 3
Traditional stationary target Imaging Method with AMD	1.484	1.540	1.517
SOA AMDIA	1.518	1.618	1.539
Proposed MTIm-AMD Method	1.396	1.410	1.399

comparing the three different AMD-SAR imaging methods are marked in red.

The IE values are consistent with the previous theoretical analysis. The proposed MTIm-AMD method received the best focus performance in all motion cases, while the SOA AMDIA obtained the worst IE results.

V. CONCLUSION

In this article, we proposed a novel moving target imaging method with the AMD echo, namely the MTIm-AMD method, to solve the problem of moving target imaging from an incomplete echo. Above all, the proposed method's effectiveness has been verified and its imaging performance advantage has been analyzed. Compared with the SOA imaging methods, the approach can outstandingly improve the final imaging result's quality in the AMD echo situation and obtain almost identical image to that of the cooperative imaging result obtained by complete echo.

Simulation results demonstrated that the noncooperative moving target can become fine imaging when the echo SNR is larger than -20 dB and the AMR is less than 70%. This implies that the proposed moving target imaging method illustrates satisfactory robustness to the echo SNR and can deal with most cases of AMD situations. Furthermore, we designed and implemented a real measured 77-GHz millimeter-wave SAR experiment for the moving target, validating the proposed method's effectiveness using real SAR data. It can facilitate further imaging algorithms, experiments, and applications for moving target SAR imaging.

However, since we first investigated the incomplete echo moving target imaging problem in this article, our proposed method only considers the uniform motion situation. The incomplete echo SAR imaging for more complex target moving models, or the moving target based on more complex SAR configurations will be a logical next step for our further works [20], [23], [24], [25], [26].

REFERENCES

[1] W. M. Brown, "Synthetic aperture radar," *IEEE Trans. Aerosp. Electron. Syst.*, vol. AES-3, no. 2, pp. 217–229, Mar. 1967.

[2] J. Yang, X. Huang, T. Jin, J. Thompson, and Z. Zhou, "Synthetic aperture radar imaging using stepped frequency waveform," *IEEE Trans. Geosci. Remote Sens.*, vol. 50, no. 5, pp. 2026–2036, May 2012.

[3] J. Wu, D. Feng, J. Wang, and X. Huang, "SAR imaging from azimuth missing raw data via sparsity adaptive StOMP," *IEEE Geosci. Remote Sens. Lett.*, vol. 19, 2022, Art. no. 4501605, doi: 10.1109/LGRS.2021.3132499.

[4] N. Jiang, D. Feng, J. Wang, and X. Huang, "Missing data SAR imaging algorithm based on two dimensional frequency domain recovery," in *Proc. IEEE Int. Geosci. Remote Sening Symp.*, 2022.

[5] J. Salzman, D. Akamine, R. Lefevre, and J. C. Kirk, "Interrupted synthetic aperture radar (SAR)," *IEEE Aerosp. Electron. Syst. Mag.*, vol. 17, no. 5, pp. 33–39, May 2002.

[6] J. Li and P. Stoica, "An adaptive filtering approach to spectral estimation and SAR imaging," *IEEE Trans. Signal Process.*, vol. 44, no. 6, pp. 1330–1334, Jun. 1996.

[7] P. Stoica, E. G. Larsson, and J. Li, "Adaptive filter-bank approach to restoration and spectral analysis of gapped data," *Astronomical J.*, vol. 120, no. 4, 2000, Art. no. 2163.

[8] E. G. Larsson, P. Stoica, and J. Li, "Amplitude spectrum estimation for two-dimensional gapped data," *IEEE Trans. Signal Process.*, vol. 50, no. 6, pp. 1343–1354, Jun. 2002.

[9] Y. Wang, P. Stoica, J. Li, and T. L. Marzetta, "Nonparametric spectral analysis with missing data via the EM algorithm," *Digit. Signal Process.*, vol. 15, no. 2, pp. 191–206, 2005.

[10] P. Stoica, J. Li, J. Ling, and Y. Cheng, "Missing data recovery via a nonparametric iterative adaptive approach," in *Proc. IEEE Int. Conf. Acoust. Speech Signal Process.*, 2009, pp. 3369–3372.

[11] D. L. Donoho, "Compressed sensing," *IEEE Trans. Inf. Theory*, vol. 52, no. 4, pp. 1289–1306, Apr. 2006.

[12] E. J. Candès, J. Romberg, and T. Tao, "Robust uncertainty principles: Exact signal reconstruction from highly incomplete frequency information," *IEEE Trans. Inf. Theory*, vol. 52, no. 2, pp. 489–509, Feb. 2006.

[13] J. Yang, J. Thompson, X. Huang, T. Jin, and Z. Zhou, "Random-frequency SAR imaging based on compressed sensing," *IEEE Trans. Geosci. Remote Sens.*, vol. 51, no. 2, pp. 1330–1334, Feb. 2012.

[14] J. Yang, J. Thompson, X. Huang, T. Jin, and Z. Zhou, "Segmented reconstruction for compressed sensing SAR imaging," *IEEE Trans. Geosci. Remote Sens.*, vol. 51, no. 7, pp. 1330–1334, Jul. 2013.

[15] H. Bi, G. Bi, B. Zhang, W. Hong, and Y. Wu, "From theory to application: Real-time sparse SAR imaging," *IEEE Trans. Geosci. Remote Sens.*, vol. 58, no. 4, pp. 2928–2936, Apr. 2020.

[16] Y. Qian and D. Zhu, "High-resolution SAR imaging from azimuth periodically gapped raw data via generalised orthogonal matching pursuit," *Electron. Lett.*, vol. 54, no. 21, pp. 1330–1334, 2018.

[17] Y. Qian and D. Zhu, "Image formation of azimuth periodically gapped SAR raw data with complex deconvolution," *Remote Sens.*, vol. 11, no. 22, 2019, Art. no. 2698.

[18] K. Liu, W. Yu, and J. Lv, "Azimuth interrupted FMCW SAR for high-resolution imaging," *IEEE Geosci. Remote Sens. Lett.*, vol. 19, 2022, Art. no. 4001105, doi: 10.1109/LGRS.2020.3019047.

[19] K. Liu, W. Yu, J. Lv, and Z. Tang, "Parameter design and imaging method of spaceborne azimuth interrupted FMCW SAR," *IEEE Geosci. Remote Sens. Lett.*, vol. 19, 2022, Art. no. 4015505, doi: 10.1109/LGRS.2021.3095173.

[20] J. Li, D. An, W. Wang, Z. Zhou, and M. Chen, "A novel method for single-channel CSAR ground moving target imaging," *IEEE Sensors J.*, vol. 19, no. 19, pp. 8642–8649, Oct. 2019.

[21] J. Wang, S. Kwon, and B. Shim, "Generalized orthogonal matching pursuit," *IEEE Trans. Signal Process.*, vol. 60, no. 12, pp. 6202–6216, Dec. 2012.

[22] S. Barbarossa and A. Farina, "Detection and imaging of moving objects with synthetic aperture radar. Part 2: Joint time-frequency analysis by Wigner-Ville distribution," *IEE Proc. F—Radar Signal Process.*, vol. 139, pp. 1330–1334, 1992.

[23] M. Newey, G. R. Benitz, D. J. Barrett, and S. Mishra, "Detection and imaging of moving targets with limit SAR data," *IEEE Trans. Geosci. Remote Sens.*, vol. 56, no. 6, pp. 3499–3510, Jun. 2018.

[24] S. Zhang, Y. Liu, X. Li, and G. Bi, "Bayesian high resolution range profile reconstruction of high-speed moving target from under-sampled data," *IEEE Trans. Image Process.*, vol. 29, pp. 5110–5120, 2022, doi: 10.1109/TIP.2020.2980149.

[25] H. An, J. Wu, K. C. Teh, Z. Sun, and J. Yang, "Simultaneous moving and stationary target imaging for geosynchronous spaceborne-airborne bistatic SAR based on sparse separation," *IEEE Trans. Geosci. Remote Sens.*, vol. 59, no. 8, pp. 6722–6735, Aug. 2021.

[26] Y. Zhang, W. Xiong, X. Dong, and C. Hu, "A novel azimuth spectrum reconstruction and imaging method for moving targets in geosynchronous spaceborne–airborne bistatic multichannel SAR," *IEEE Trans. Geosci. Remote Sens.*, vol. 58, no. 8, pp. 5976–5991, Aug. 2020.

Nan Jiang received the B.S. degree in electronic information engineering and the M.S. degree in information and communication engineering, both from the University of Electronic Science and Technology of China, Chengdu, China, in 2016 and 2019, respectively. He is currently working toward the Ph.D. degree in information and communications engineering with the National University of Defense Technology, Changsha, China.

His research interests include radar signal processing and compressed sensing.

Jian Wang received the B.S., M.S., and Ph.D. degrees in information and communications engineering from the National University of Defense Technology, Changsha, China, in 2003, 2004 and 2009, respectively.

He is currently a Lecturer with the National University of Defense Technology. His research interests include ground surveillance radar, target tracking, SAR image formation, and SAR interferometry.

Dong Feng received the B.S. degree in information engineering, and the M.S. and Ph.D. degrees in information and communication engineering from the National University of Defense Technology, Changsha, China, in 2013, 2015 and 2020, respectively.

He is currently a Lecturer with the National University of Defense Technology. His research interests include bistatic SAR image formation and holographic SAR 3-D image formation.

Naixin Kang received the B.S. and M.S. degrees in electronic countermeasure engineering from Air Force Early Warning Academy, Wuhan, China, in 2014 and 2016, respectively. She is currently working toward the Ph.D. degree in information and communication engineering with the National University of Defense Technology, Changsha, China.

Her research interests include radar signal processing and imaging technology.

Xiaotao Huang (Senior Member, IEEE) received the B.S. and Ph.D. degrees in information and communications engineering from the National University of Defense Technology, Changsha, China, in 1990 and 1999, respectively.

He is currently a Professor with the National University of Defense Technology. His research interests include radar theory, signal processing, and radio frequency signal suppression.